Available online at www.sciencedirect.com
ScienceDirect
International Journal of Heat and Mass Transfer 51 (2008) 3882–3895
International Journal of HEAT and MASS TRANSFER
www.elsevier.com/locate/ijhmt

Single-phase and two-phase heat transfer characteristics of low temperature hybrid micro-channel/micro-jet impingement cooling module

Myung Ki Sung, Issam Mudawar *

Boiling and Two-Phase Flow Laboratory (BTPFL), Purdue University International Electronic Cooling Alliance (PUIECA), Mechanical Engineering Building, 585 Purdue Mall, West Lafayette, IN 47907-2088, USA

Received 23 July 2007; received in revised form 19 December 2007
Available online 17 March 2008

Abstract

This study examines the single-phase and two-phase cooling performance of a hybrid micro-channel/micro-jet impingement cooling scheme using HFE 7100 as working fluid. This scheme consists of supplying coolant from a series of jets that deposit liquid into the micro-channels. A single-phase numerical scheme that utilizes the k–ε turbulent model and a method for determining the extent of the laminarized wall layer shows very good predictions of measured wall temperatures. It is shown jet velocity has a profound influence on single-phase cooling performance. High jet velocities enable jet fluid to penetrate the axial micro-channel flow and produce a strong impingement effect at the wall. On the other hand, the influence of jets at low jet velocities is greatly compromised compared to the micro-channel flow. During nucleate boiling, vapor layer development along the micro-channel in the hybrid module is fundamentally different from that encountered in conventional micro-channels. Here, subcooled jet fluid produces repeated regions of bubble growth followed by bubble collapse, rather than the continuous growth common to conventional micro-channel flow. By reducing void fraction along the micro-channel, the hybrid scheme contributes greater wall temperature uniformity. Increasing subcooling and/or flow rate delay the onset of boiling to higher heat fluxes and higher wall temperatures, and also increase critical heat flux considerably. A nucleate boiling heat transfer coefficient correlation is developed that fits the present data with a mean absolute error of 6.10%.

1. Introduction

Accurate prediction of pressure drop and heat transfer characteristics is essential to the effective design of a cooling module that is intended for high-heat-flux removal in such applications as high performance microprocessors, laser diode arrays, radars and X-ray anodes [1]. This paper is a follow-up to a recent study by the present authors in which a hybrid cooling scheme was proposed for such applications [2]. This scheme combines the cooling benefits of micro-channel flow and micro-jet impingement, as well as takes advantage of indirect refrigeration cooling. Unlike the prior study, which explored only the single-phase heat transfer performance of the hybrid scheme for relatively low Reynolds number jets, the present paper both extends the single-phase findings to high Reynolds numbers and explores the module's two-phase cooling characteristics.

Three-dimensional numerical modeling is a highly effective tool for predicting both the complex flow interactions occurring inside the hybrid cooling module, and the module's single-phase cooling performance. Prior to the above-mentioned study by the authors, no modeling of this hybrid cooling configuration has been attempted. However, researchers have examined micro-channel flow and jet impingement independently. For example, Fedorov and Viskanta [3] developed a three-dimensional model to predict the development of both velocity and temperature fields in a micro-channel heat sink. Qu and Mudawar [4]

* Corresponding author. Tel.: +1 765 494 5705; fax: +1 765 494 0539.
E-mail address: mudawar@ecn.purdue.edu (I. Mudawar).

0017-9310/$ - see front matter © 2008 Elsevier Ltd. All rights reserved.
doi:10.1016/j.ijheatmasstransfer.2007.12.016

Nomenclature

A_t	area of copper block's top test surface
c	constant in Eq. (15)
C	empirical constant in Eq. (24)
C_1, C_2, C_μ	turbulence model constants
c_p	specific heat at constant pressure
D_{jet}	diameter of circular jet
G	production of turbulent energy
h	height of wall jet; two-phase convective heat transfer coefficient, $q''_{eff}/(T_s - T_{in})$
H	height of unit cell, distance between jet and heated surface
H_{ch}	height of channel
H_{jet}	height of jet
H_{th}	height from unit cell bottom boundary to thermocouple holes
H_w	height from unit cell bottom boundary to test surface
k	thermal conductivity; turbulent kinetic energy
l	parameter defined in Eq. (18)
L	length of unit cell
L_{jet}	pitch of circular jets
L_1, L_2, L_3, L_4	distance between thermocouple holes
$\dot{m}$	mass flow rate
n	coordinate normal to solid interface; empirical constant in Eq. (24)
N	number of jets in jet plate
Nu	Nusselt number
P	Pressure
Pr	Prandtl number
P_W	electrical power supplied to copper heating block
q''	heat flux
q''_{eff}	effective heat flux based on top test surface area of copper block, $q''_{eff} = P_W/A_t$
Q	volumetric flow rate
r	radius measured from point of jet impact
r_j	radius of circular jet
r_s	radius extent of stagnation zone
r_b	radial location where boundary layer reaches film thickness
r_t	critical radius corresponding to onset of turbulence zone
Re_{jet}	jet Reynolds number
T	temperature
T_{in}	jet inlet temperature
T_{tci}	temperature measured by thermocouple tc$i$ ($i = 1$ to 4)
ΔT_{sat}	superheat, $T_s - T_{sat}$
ΔT_{sub}	subcooling, $T_{sat} - T_f$
u	velocity component in x-direction
U_i	Cartesian component of velocity
U_{jet}	jet inlet velocity, $U_{jet} = Q/(NA_{jet})$
v	velocity component in y-direction
w	velocity component in z-direction
W	width of unit cell
W_{ch}	width of channel
W_w	half-width of wall separating channels
x	Cartesian coordinate
y	Cartesian coordinate
z	Cartesian coordinate

Greek symbols

δ	hydrodynamic boundary layer thickness
δ_{th}	thermal boundary layer thickness
ε	dissipation rate of turbulent kinetic energy
μ	dynamic viscosity
μ_t	eddy viscosity
ρ	density
σ_ε	empirical constant in k and ε transport equations
σ_k	empirical constant in k and ε transport equations

Subscripts

corr	correlated
exp	experimental
f	fluid
in	inlet
jet	jet
out	outlet
s	test surface
sat	saturation
sub	subcooling
t	turbulent
tc$i$	thermocouple ($i = 1$ to 4)
Γ	interface between solid and liquid

proved pressure drop and heat transfer characteristics of micro-channel heat sinks can be accurately predicted by solving the conventional Navier–Stokes and energy equations. Baydar and Ozmen [5] examined confined high Reynolds number impinging air jets using the standard k–ε turbulence model. Barata et al. [6] conducted 3-D numerical simulation of an impinging jet with a low velocity cross-flow and illustrated a scarf vortex around the jet. Craft et al. [7] tested four different turbulence models and demonstrated that the k–ε model accurately predicts the flow characteristics of impinging jets.

Phase change greatly enhances cooling performance in both micro-channel flow and jet impingement. This enhancement is of paramount importance to applications demanding the removal of large amounts of heat from very small surface areas. With single-phase liquid cooling,

increasing the heat flux produces a proportional increase in the device-to-fluid temperature difference. On the other hand, phase change produces only a mild increase in temperature difference corresponding to large increases in heat flux. This attractive cooling attribute is realized within the nucleate boiling regime provided the device heat flux is kept safely below critical heat flux (CHF).

Bowers and Mudawar [8] provided the earliest framework for designing and modeling two-phase micro-channel heat sinks. Since their study, many other studies have been published that examined performance and modeling aspects of two-phase micro-channel cooling. Qu and Mudawar [9] conducted an experimental study of two-phase micro-channel heat sinks. They observed two types of hydrodynamic instability, severe pressure oscillation and mild parallel channel instability, and provided practical guidelines to prevent the severe pressure oscillation. Lee and Mudawar [10] carried out experiments in which a two-phase micro-channel heat sink served as an evaporator in a vapor compression system using R134a as working fluid. They showed the parallel channel instability could be dampened with additional throttling upstream of the heat sink. Overall, two-phase micro-channel flow is associated with appreciable pressure drop as well as axial variations of surface temperature.

Researchers also investigated the two-phase heat transfer characteristics of impinging jets. Yang et al. [11] carried out experiments with a free circular jet impinging on a rectangular heated surface. They showed a high degree of subcooling greatly suppresses bubble growth due to condensation. Wolf et al. [12] showed the two-phase heat transfer coefficient of a free slot jet is independent of jet velocity in the fully developed nucleate boiling regime. These and other studies show high-heat transfer coefficients are possible with free circular and slot impinging jets. Unfortunately, severe boiling in the wall liquid layer emanating from the stagnation zone of a free jet has been observed to push liquid away from the surface, causing both large surface temperature gradients and premature critical heat flux (CHF) [1]. This problem can be corrected by confining the flow to the vicinity of the surface following impingement. Wadsworth and Mudawar [13] conducted single-phase and two-phase experiments with confined slot jets of subcooled FC-72 that impinged on a 12.7×12.7 mm heat source. They showed flow confinement greatly enhances both surface temperature uniformity and CHF. Another means to reduce the surface temperature gradient away from the impingement zone is to use multiple impinging jets. While multiple jets both increase overall cooling rate and reduce surface temperature gradients, they can produce such adverse effects as flow blockage between jets and instability in the flow of spent fluid, especially when jets are stacked in a large two-dimensional array.

This paper explores both the single-phase and two-phase heat transfer characteristics of a hybrid cooling scheme that capitalizes upon the merits of both micro-circular-jet impingement and micro-channel flow while avoiding their drawbacks. In a previous study by the authors [2], a parametric study of the effects of flow geometry on single-phase cooling performance was conducted in pursuit of both lower surface temperature and better surface temperature uniformity using HFE 7100 as working fluid. This paper extends the earlier findings to high jet Reynolds numbers and two-phase cooling.

2. Experimental methods

2.1. Test module

Fig. 1 illustrates the construction and assembly of the test module, which consists of a copper heating block, an upper plenum plate, a micro-jet plate, a lower support plate, and 16 cartridge heaters. The micro-channels were formed by cutting five 1 mm wide by 3 mm deep slots equidistantly within the 1.0 cm width of the top 1.0×2.0 cm^2 test surface area of the copper heating block. Heat is supplied to the test surface from the cartridge heaters, which are inserted into bores machined in the underside of the copper block. The cartridge heaters are powered by a 0-110 VAC variac, and their total power input is measured by a Yokogawa WT 210 wattmeter. Test surface temperature and heat transfer coefficient distributions are determined with aid of six copper-constantan (type-T) thermocouples inserted a small distance below the test surface.

The micro-jet plate is also machined from oxygen-free copper. Five parallel rows of fourteen 0.39 mm diameter holes are drilled equidistantly into the micro-jet plate, with each row aligned to impinge fluid along the centerline of the micro-channels. The upper plenum plate and lower support plate are fabricated from high-temperature G-11 fiberglass plastic. The inlet plenum for the jets is formed in the upper plenum plate. The copper heating block is inserted into the hollow center of the bottom support plate; the latter contains outlet plenums for the flow exiting the micro-channels. Absolute pressure transducers are connected via pressure taps to the inlet plenum and one of the two outlet plenums to measure test module inlet and outlet pressures, respectively. Also inserted into the inlet and one of the outlet plenums are two type-T thermocouples, which measure inlet and the outlet fluid temperatures, respectively. To minimize heat loss to the ambient, the heating block rests on a solid insulating ceramic plate and is encased laterally with a thick layer of ceramic fiber.

2.2. Flow loop and experimental procedure

Fig. 2 shows a schematic diagram of a flow system that delivers HFE 7100 liquid at the desired pressure, temperature and flow rate to the test module. This system consists of a primary HFE 7100 cooling loop that contains the test module, and a separate low temperature refrigeration system. Heat from the primary coolant is rejected to the refrigeration system via a heat exchanger. The refrigeration system uses feedback control to regulate the temperature

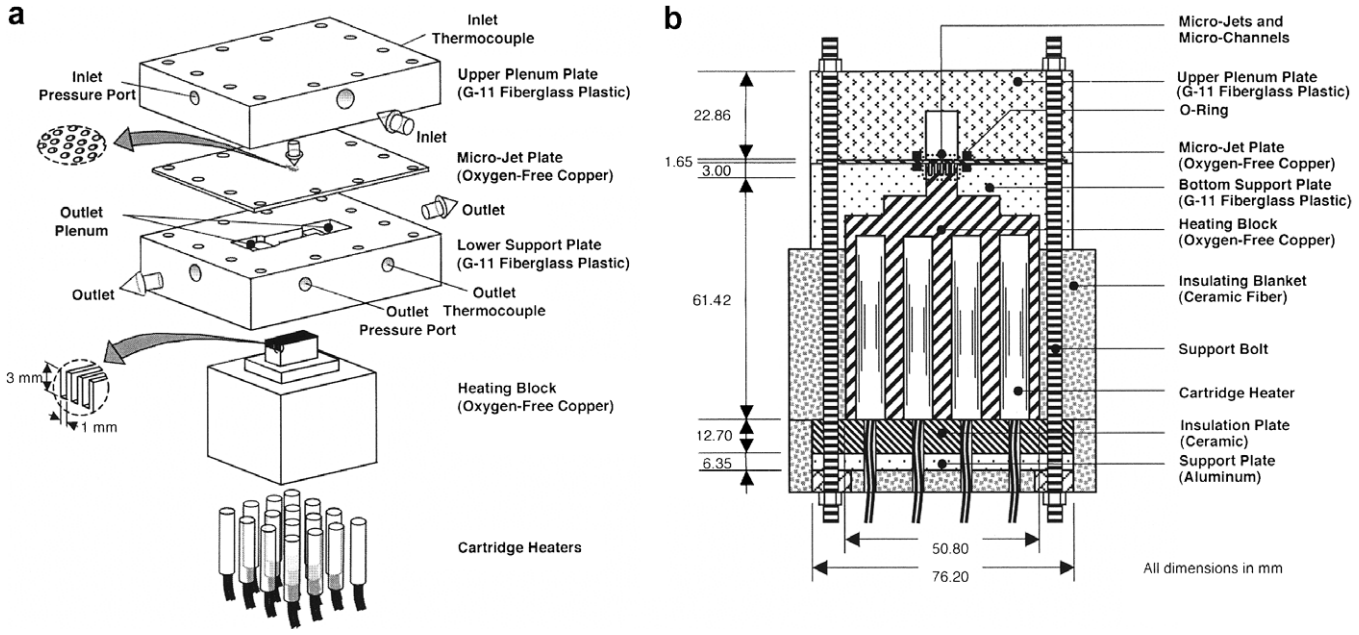

Fig. 1. (a) Test module construction. (b) Cross-section of module assembly.

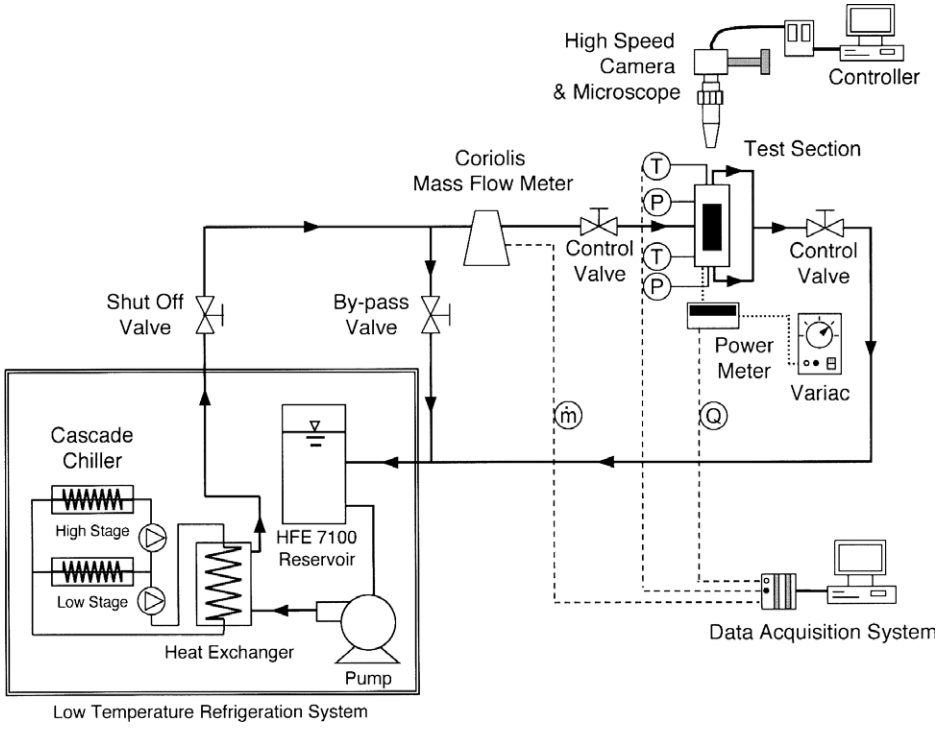

Fig. 2. Schematic of flow system.

of HFE 7100 liquid exiting the heat exchanger to within ±0.5 °C. In the primary loop, flow rate and pressure are regulated with the aid of control values situated upstream and downstream of the test module, as well as a bypass valve. The flow rate of HFE 7100 is measured by a Coriolis flow meter.

After the desired test module inlet conditions are reached, data are recorded after increasing electrical power input to the test module in small increments. Once steady-state is reached following each power increment, the module inlet pressure, P_{in}, outlet pressure, P_{out}, inlet temperature, T_{in}, outlet temperature, T_{out}, heating block temperatures, T_{tc1} to T_{tc4}, and heater power, P_W, are recorded for later processing. Measurement uncertainties associated with the pressure transducers, flow meter, wattmeter, and thermocouples are 0.5%, 0.1%, 0.5%, and 0.3 °C, respectively. Heat

Table 1
Experimental operating conditions

Working fluid	Inlet temperature $T_{in}(°C)$	Jet velocity $U_{jet}(m/s)$	Outlet pressure P_{out}(bar)	Effective heat flux q''_{eff} (W/cm^2)
HFE 7100	−40 to 20	0.85 to 4.70	1.31 to 1.67	16.06 to 311.00

loss is estimated at less than 8% of the total power input. All test module heat fluxes reported in this study are therefore based on electrical power input. Table 1 lists the experimental operating conditions of the study.

3. Numerical methods

3.1. Computational scheme

Fig. 3 shows a unit cell that was used to construct a computational model of single-phase cooling behavior of the hybrid micro-channel/micro-jet module. The unit cell consists of a single micro-channel, micro-jets impinging in the same micro-channel, and surrounding solid. Due to symmetry, a computational domain consisting of only one quarter of the unit cell is required. Table 2 provides key dimensions of the unit cell.

FLUENT 6.2.16 [14] and is used to compute flow profiles and heat transfer characteristics of the hybrid module. The computational grid is constructed using Gambit 2.2.30 [15]. The standard two-equation k–ε turbulent model [16] is applied for closure of the Reynolds stress tensor.

The governing conservation equations for steady, turbulent and incompressible flow with constant properties are expressed as follows.

For the fluid region,

$$\frac{\partial U_i}{\partial x_i} = 0, \tag{1}$$

$$\rho_f U_j \frac{\partial U_i}{\partial x_j} = -\frac{\partial P}{\partial x_i} + \frac{\partial}{\partial x_j}\left((\mu_f + \mu_t)\frac{\partial U_i}{\partial x_j}\right), \tag{2}$$

$$\text{and} \quad \rho_f c_{p,f} U_j \frac{\partial T}{\partial x_j} = \frac{\partial}{\partial x_j}\left(\left(k_f + \frac{c_{p,f}\mu_t}{Pr_t}\right)\frac{\partial T}{\partial x_j}\right), \tag{3}$$

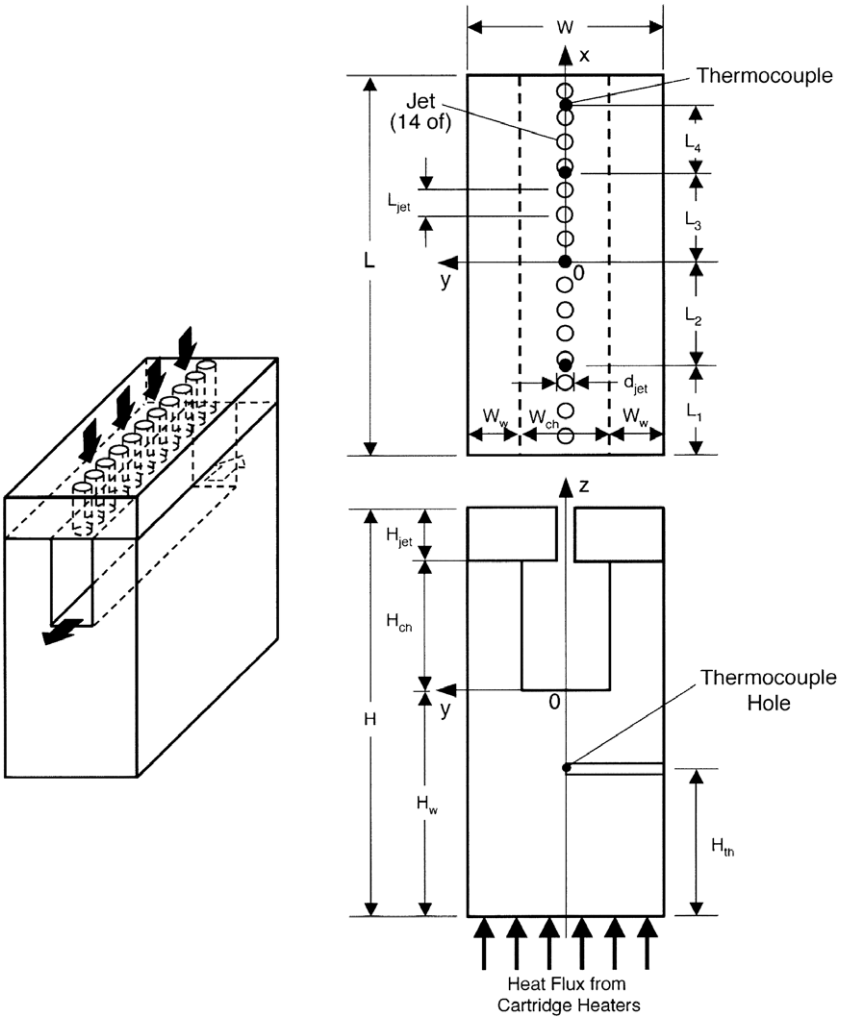

Fig. 3. Schematic of unit cell consisting of row of micro-jets and single micro-channel.

Table 2
Dimensions of unit cell

L (mm)	L_1 (mm)	L_2 (mm)	L_3 (mm)	L_4 (mm)	W (mm)	W_{ch} (mm)	W_w (mm)	H (mm)	H_{jet} (mm)	H_{ch} (mm)	H_w (mm)	H_{th} (mm)	D_{jet} (mm)	L_{jet} (mm)
20.00	4.00	6.00	3.00	6.00	1.83	1.00	0.42	14.27	1.65	3.00	7.62	5.08	0.39	1.43

$$\text{where} \quad \mu_t = \frac{C_\mu \rho_f k^2}{\varepsilon}, \tag{4}$$

$$\rho_f U_j \frac{\partial k}{\partial x_j} = \frac{\partial}{\partial x_j}\left(\left(k_f + \frac{\mu_t}{\sigma_k}\right)\frac{\partial k}{\partial x_j}\right) + G - \rho_f \varepsilon, \tag{5}$$

$$\text{and} \quad \rho_f U_j \frac{\partial \varepsilon}{\partial x_j} = \frac{\partial}{\partial x_j}\left(\left(k_f + \frac{\mu_t}{\sigma_\varepsilon}\right)\frac{\partial \varepsilon}{\partial x_j}\right) + C_1 G\frac{\varepsilon}{k} - C_2 \rho_f \frac{\varepsilon^2}{k}. \tag{6}$$

The production of turbulent energy is defined as $G = -\overline{u_i u_j}\partial U_i/\partial x_j$. The following values are used for the coefficients in the above equations: $C_\mu = 0.09$, $C_1 = 1.44$, $C_2 = 1.92$, $\sigma_k = 1.0$, $\sigma_\varepsilon = 1.3$, and $Pr_t = 0.85$.

For the solid region,

$$U_i = 0, \tag{7}$$

$$\text{and} \quad \frac{\partial}{\partial x_j}\left(k_s \frac{\partial T}{\partial x_j}\right) = 0. \tag{8}$$

Boundary conditions are specified as follows.

$$\text{Jet inlet}: u = 0, \quad v = 0, \quad w = -w_{in}, \quad \text{and } T = T_{in}. \tag{9}$$

$$\text{Micro-channel outlet}: \dot{m} = \dot{m}_{in}, \quad \frac{\partial v}{\partial x} = 0, \quad \frac{\partial w}{\partial x} = 0,$$

$$\text{and } \frac{\partial T}{\partial x} = 0. \tag{10}$$

A constant heat flux is applied along the bottom of the unit cell

$$-k_s \frac{\partial T}{\partial z} = q''_{eff}, \tag{11}$$

where q''_{eff} is determined from the measured electrical power input

$$q''_{eff} = \frac{P_W}{A_t}. \tag{12}$$

Adiabatic conditions are applied to the outer solid region boundaries except for interfaces between fluid and solid. The SIMPLE (Semi-Implicit Method for Pressure-Linked Equations) algorithm by Patankar [17] is applied to couple velocities and pressure.

Three different mesh sizes were tested using 195,720, 414,656 and 693,500 elements. The middle mesh size is employed in this study because temperature differences between the two finer mesh sizes are less than 2.27%.

3.2. Determination of extent of laminar zone

Two concerns in implementing the numerical methods described in Ref. [2] are (1) the suitability of the standard k–ε model to complex interactions of high Reynolds number jets with parallel channel flow, and (2) determination of the radial extent from the jet's stagnation point where the turbulent zone commences.

To determine the upstream radial location of the turbulent zone, laminar flow is imposed on the computational domain from the jet inlet to the stagnation zone, and a portion of the wall jet surrounding the stagnation zone. The computational domain in FLUENT is therefore divided into two sub-zones, a laminar zone and a turbulent zone.

Determining the extent of the laminar zone away from the stagnation zone based on first principles is quite elusive. However, significant insight may be gained from a related flow configuration involving a free circular impinging liquid jet.

For a circular free jet, Fig. 4 shows the flow field along a heated surface can be classified into four regions: a stagnation zone, a boundary layer region, a similarity or fully viscous region and a turbulent region. Within the stagnation zone, the circular jet flow decelerates normal to the surface but accelerates radially, and the flow is laminarized by a strong radial pressure gradient [18]. Watson [19] used inviscid theory to determine thickness h of the wall jet on the surface in the stagnation zone. For inviscid Bernoulli flow, mass conservation yields

$$\frac{\pi D_{jet}^2}{4} U_{jet} = 2\pi r h U_{jet}, \tag{13}$$

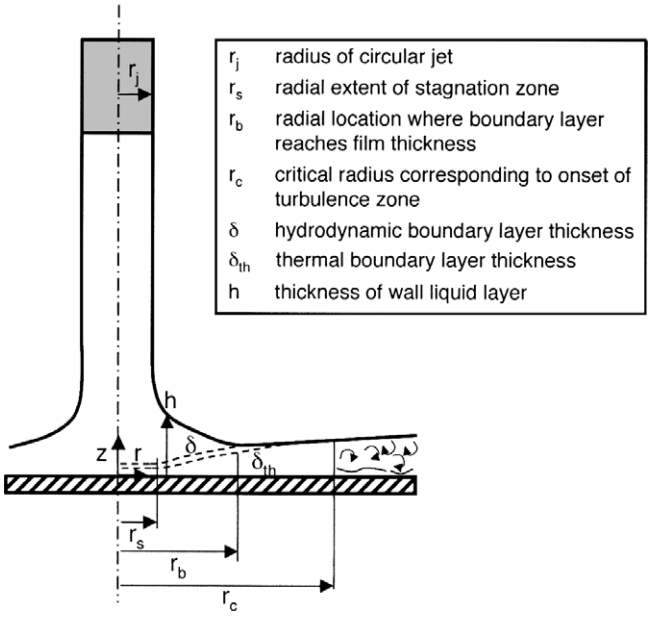

Fig. 4. Fluid flow regimes for free circular impinging jet with $Pr_f > 1$.

which can be simplified into

$$h = \frac{D_{jet}^2}{8r} \text{ for } 0 < r < r_s. \tag{14}$$

Jet flow in the boundary layer region is not entirely influenced by wall friction. Watson [19] obtained the following approximate solution for the developing boundary layer region by solving the momentum integral equation for boundary layer thickness based on an assumed velocity profile.

$$h = \left(\frac{D_{jet}^2}{8r}\right) + \left\{1 - \frac{2\pi}{3\sqrt{3}c^2}\right\}\delta \text{ for } r_s < r < r_b, \tag{15}$$

where

$$\delta^2 = \frac{\sqrt{3}c^3}{\pi - c\sqrt{3}} \frac{r}{D_{jet}Re_{jet}} \text{ and } c = 1.402. \tag{16}$$

In the fully viscous region, hydrodynamic boundary layer thickness is the same as the thickness of liquid wall layer, $\delta = h$. Here, viscous effects extend across the entire liquid film, and the mean liquid velocity decreases with r. Watson derived the following relation for liquid layer thickness in this region based on a similarity velocity profile with a Jacobi elliptic function.

$$h = \frac{8\pi}{3\sqrt{3}} \frac{\left(r^3 + l^3\right)}{D_{jet}Re_{jet}r}, \text{ for } r_b < r < r_c, \tag{17}$$

$$\text{where } \quad l = 0.3296 D_{jet}Re_{jet}^{1/3}. \tag{18}$$

The radius between the developing boundary layer region and fully viscous region is given as

$$r_b = 0.1834 D_{jet}Re_{jet}^{1/3}. \tag{19}$$

Returning to the present hybrid cooling configurations, it must be noted that, for the minimum jet velocity tested of $U_{jet} = 2.68$ m/s, the distance L_{jet} between jets feeding liquid into a single micro-channel is shorter than radius r_b, where the fully viscous region begins. This means only the stagnation and boundary layer regions of the wall liquid layer are of importance. Therefore, laminar flow is imposed on the flow domain between the jet inlet and stagnation zone, as well as up to height $h(r)$ from the wall as given by Eqs. (14) and (15). Turbulence is permitted everywhere else in the computational domain.

4. Single-phase heat transfer characteristics

4.1. Comparison of numerical predictions with experimental results

Fig. 5 compares numerical predictions of the temperature distribution along the thermocouple line inside the copper heating block with the thermocouple measurements. Both the numerical predictions and experimental data show wall temperature decreases with decreasing liquid inlet temperature for about the same jet velocity and wall heat flux. Both predictions and experimental data also show strong influence of jet velocity on cooling performance. For an inlet temperature of $T_{in} = 0$ °C, Fig. 5 shows increasing jet velocity from $U_{jet} = 2.68$ to 4.53 m/s, facilitates the removal of nearly twice the wall heat flux while incurring only a mild axial increase in the wall temperature.

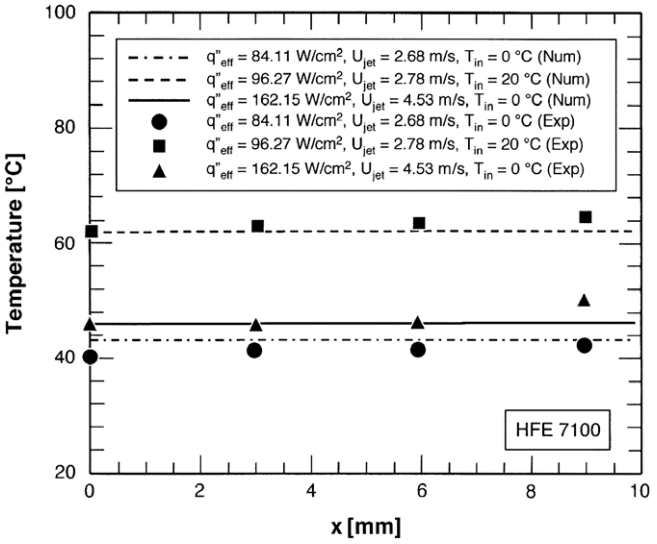

Fig. 5. Comparison of numerical predictions of temperatures along thermocouple line with measured temperatures.

Close agreement between predicted and measured temperatures proves the single-phase performance of the present hybrid cooling scheme can be accurately predicted with the Navier–Stokes and energy equations using the standard k–ε model, which is consistent with authors' previous work [2]. This agreement also demonstrates the effectiveness of the technique discussed earlier for determining the extent of the laminar zone of the computational domain.

4.2. Parametric trends of cooling characteristics

Table 3 summarizes the different numerical simulation tests that were used to examine the cooling performance of the hybrid cooling scheme.

Fig. 6a and b show predicted temperature distributions along the micro-channel's bottom wall for $q''_{eff} = 53.39$ W/cm^2 and $U_{jet} = 0.90$ m/s, and $q''_{eff} = 162.15$ W/cm^2 and $U_{jet} = 4.53$ m/s, respectively. For the weaker jet case, Fig. 6a, heat transfer appears to be dominated more by the micro-channel flow than by jet impingement. Since

Table 3
Numerical simulation cases using HFE 7100 as working fluid

Inlet temperature T_{in} (°C)	Flow rate Q (m^3/s)	Jet velocity U_{jet} (m/s)	Effective heat flux q''_{eff} (W/cm^2)
0	7.34×10^{-6}	0.90	53.39
20	2.19×10^{-5}	2.68	84.11
0	2.28×10^{-5}	2.78	96.27
0	3.71×10^{-5}	4.53	162.15

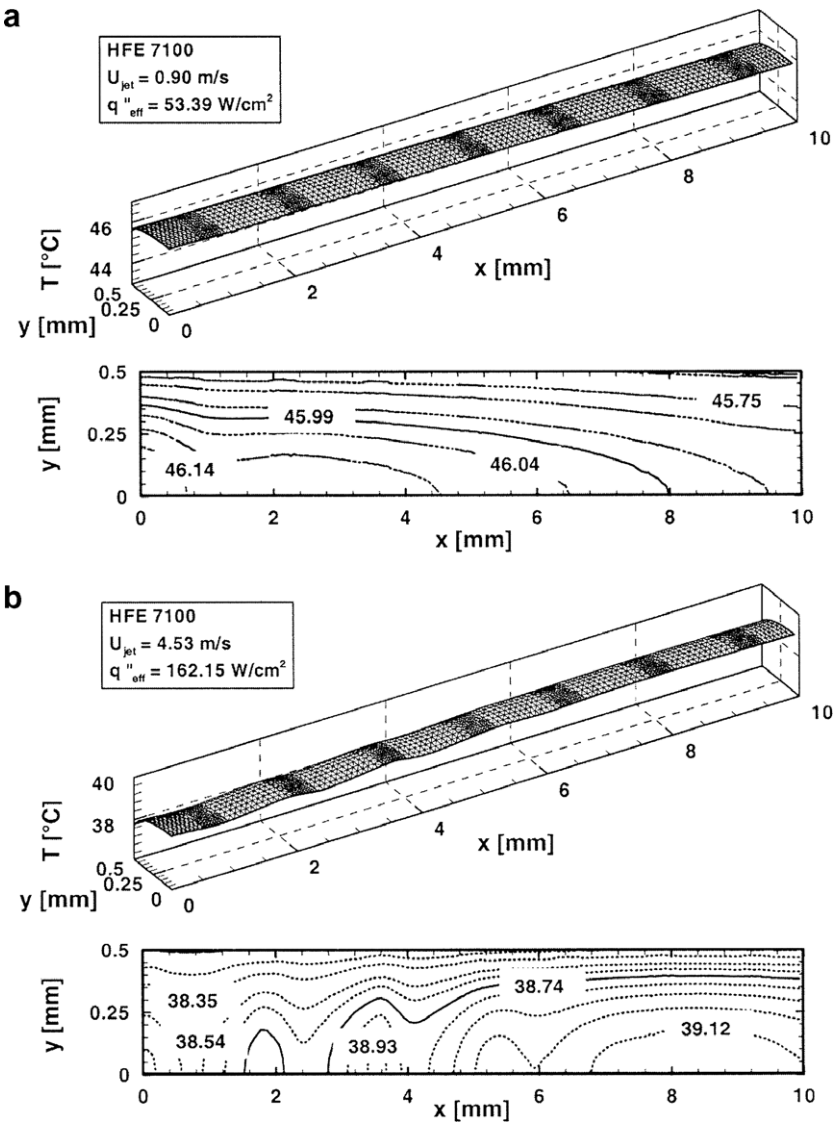

Fig. 6. Numerical predictions of micro-channel bottom wall temperature distribution for (a) $q''_{\text{eff}} = 53.39\ \text{W/cm}^2$ and $U_{\text{jet}} = 0.90\ \text{m/s}$, and (b) $q''_{\text{eff}} = 162.15\ \text{W/cm}^2$ and $U_{\text{jet}} = 4.53\ \text{m/s}$.

coolant flow rate increases along the flow direction, the heat transfer coefficient is highest and wall temperature lowest near the outlet ($x = 10$ mm). The reverse is true for the stronger jet case, Fig. 6b. Here, heat transfer appears to be influenced more by jet impingement than by the micro-channel flow, evidenced by both the local depressions in wall temperature immediately below the jets as well as the lower overall wall temperatures. Due to the fin effect of the micro-channel sidewall, lower temperatures are achieved along the corner of the micro-channel's bottom wall for both the weak and the strong jet cases.

Fig. 7 shows bottom wall temperature distribution including the region below the micro-channel sidewall. Temperature profiles are shown for four different axial locations, $x = 0$, 3, 6, and 9 mm. These profiles depict the aforementioned fin effect of the micro-channel sidewall. Small variations between temperature profiles corresponding to different axial locations highlight the effectiveness of the hybrid cooling scheme at virtually eliminating the axial temperature gradients often associated with conventional micro-channel heat sinks.

Fig. 8 shows further evidence of the relative contributions of jets and micro-channel flow for weak and strong jets. Streamline plots in Fig. 8a corresponding to weak jets show the jet flow is barely able to penetrate the axial micro-channel flow and have its effect felt at the wall. This is especially the case for downstream jets that face increasing resistance from the gradually increasing micro-channel flow. On the other hand, Fig. 8b shows jets are better able to penetrate the micro-channel and produce a strong impingement effect at the wall. Despite the increasing micro-channel flow in the x-direction, Fig. 8b shows the jet fluid approaching the wall for most jets, though downstream jets appear to be facing greater resistance from the micro-channel flow. This strong impingement effect is manifest in Fig. 6 in the form of greater heat transfer coefficients.

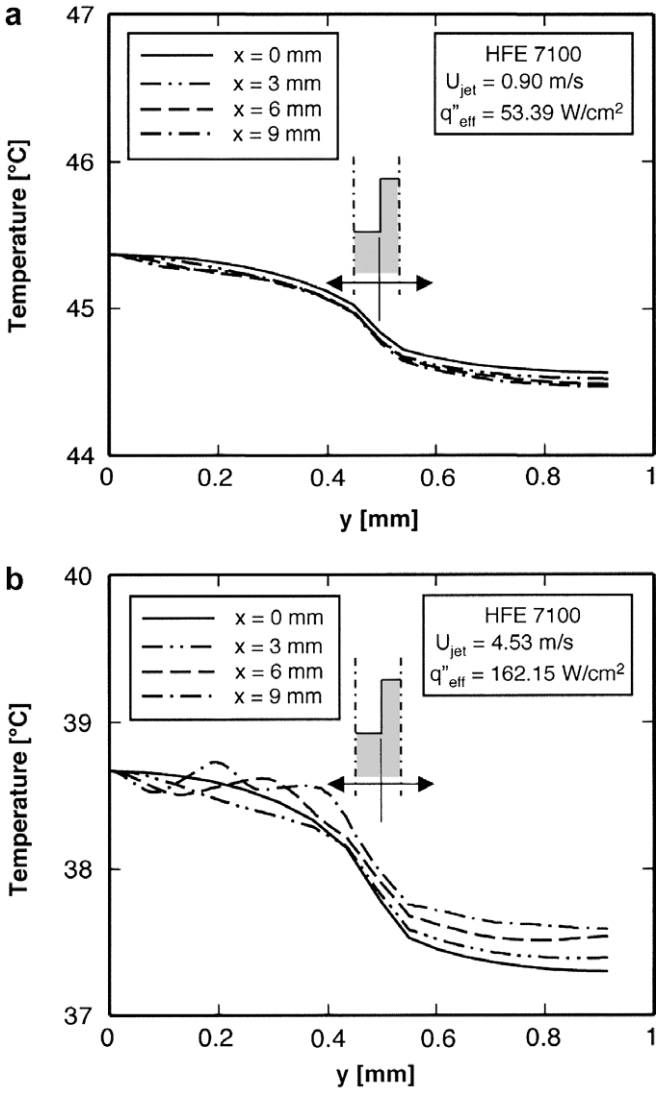

Fig. 7. Numerical predictions of wall temperature, including sidewall region, at four axial locations for (a) $q''_{\text{eff}} = 53.39\ \text{W/cm}^2$ and $U_{\text{jet}} = 0.90$ m/s, and (b) $q''_{\text{eff}} = 162.15\ \text{W/cm}^2$ and $U_{\text{jet}} = 4.53$ m/s.

These trends are further illustrated in plots of heat flux distribution along the bottom wall of the micro-channel. These distributions are shown for weak and strong jet cases in Figs. 9a and b, respectively. In these plots, local heat flux is evaluated as

$$q'' = -k_{\Gamma}\left.\frac{\partial T_{\Gamma}}{\partial n}\right|_{\Gamma}, \tag{20}$$

where k_{Γ} is the interface thermal conductivity obtained by the harmonic mean of k_s and k_f. Both figures show higher heat fluxes are encountered near the jet centerline, but this effect is more noticeable for the strong jets. Heat flux is quite small in the corner of the micro-channel where the flow is weakest. For the weak jet case, Fig. 9a, the highest heat flux is encountered near the first jet closest to the center of the micro-channel, and the lowest heat flux near the micro-channel center ($x = 0$). Notice that local heat flux peaks are dampened by the micro-channel flow for all jets excepting the most upstream. On the other hand, Fig. 9b shows strong jets produce noticeable local peaks in the heat flux distribution for several upstream jets. However, the peaks are ultimately dampened for the three most downstream jets.

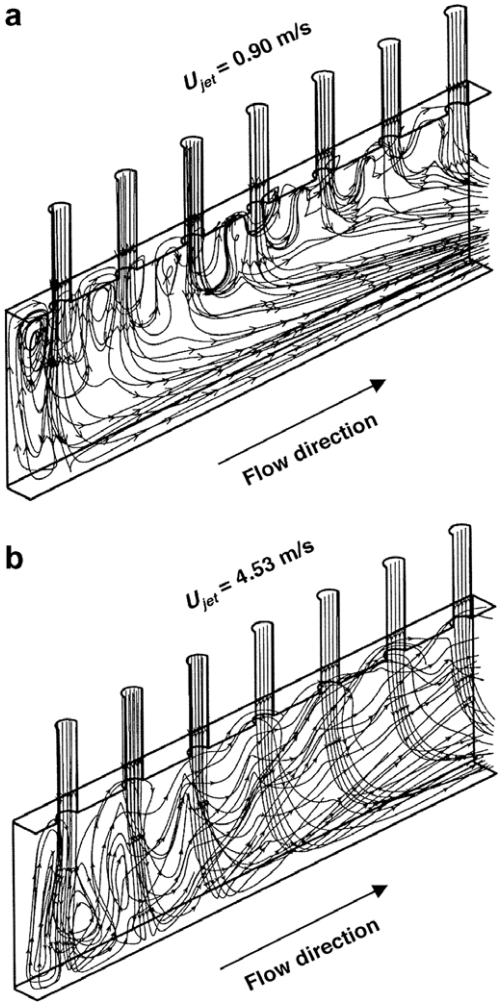

Fig. 8. Streamline plots for (a) $U_{\text{jet}} = 0.90$ m/s and (b) $U_{\text{jet}} = 4.53$ m/s.

Similar trends are shown in Fig. 10 in the form of Nusselt number distribution along the bottom wall, where the local Nusselt number is defined as

$$Nu = \frac{q'' L_{\text{jet}}}{k_f (T_s - T_{\text{in}})}. \tag{21}$$

5. Two-phase heat transfer characteristics

5.1. Boiling curve trends

Fig. 11a and b shows boiling curves for the present hybrid cooling module for $U_{\text{jet}} = 0.9$ m/s and inlet subcoolings of $\Delta T_{\text{sub}} = 88.7$ and 48.2 °C, respectively. Wall temperature data are shown for $x_{\text{tc1}} = 0.0$, $x_{\text{tc2}} = 3.0$, $x_{\text{tc3}} = 6.0$, and $x_{\text{tc4}} = 9.0$ mm from the center of the micro-channel. Each temperature is determined from the applied heat flux, q''_{eff}, and the thermocouple measurement at the same

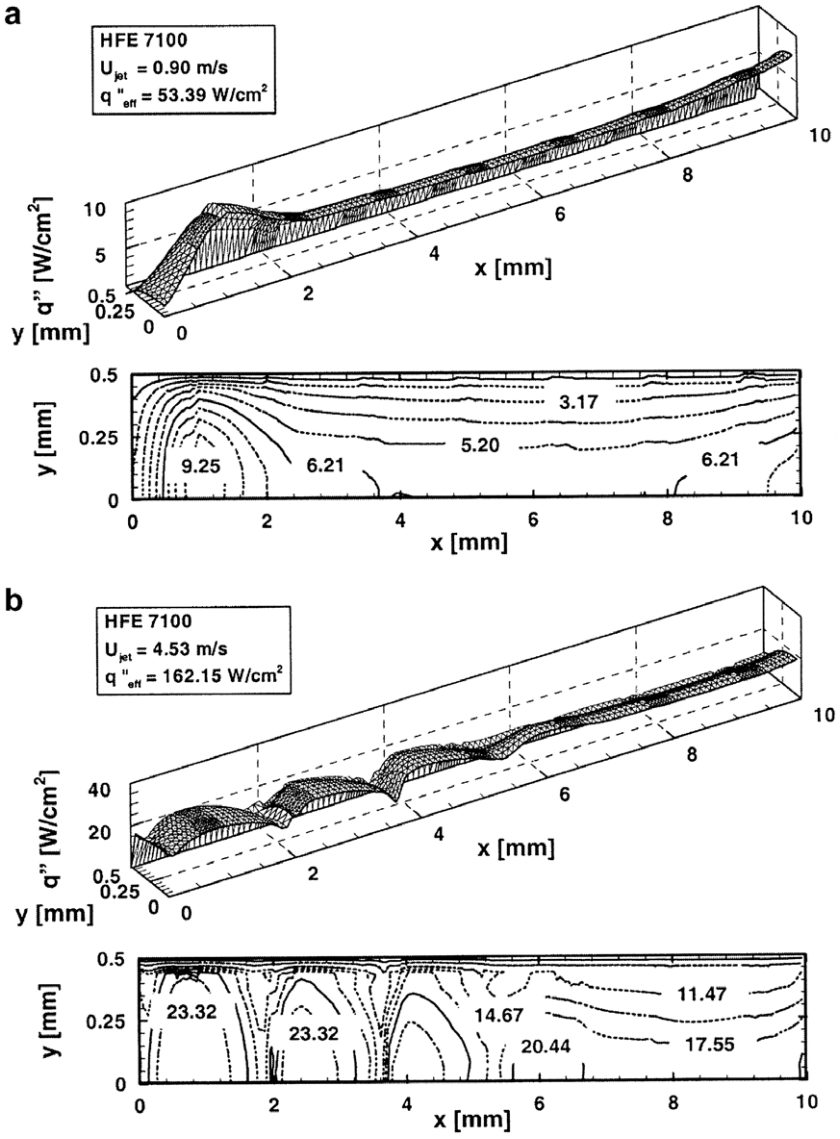

Fig. 9. Numerical predictions of micro-channel bottom wall heat flux distribution for (a) $q''_{\text{eff}} = 53.39\ \text{W/cm}^2$ and $U_{\text{jet}} = 0.90\ \text{m/s}$ and (b) $q''_{\text{eff}} = 162.15\ \text{W/cm}^2$ and $U_{\text{jet}} = 4.53\ \text{m/s}$.

axial location by assuming one-dimensional heat conduction between the thermocouple and the micro-channel's bottom wall. The inlet temperature, T_{in}, is measured by the thermocouple inserted in the inlet plenum.

At low heat fluxes corresponding to single-phase heat transfer, Fig. 11a and b shows fairly constant slopes for all boiling curves. With increasing heat flux, different trends are observed, depending on the magnitude of subcooling. Fig. 11b shows the slope begins to increase at x_{tc4}, the most downstream of the four wall locations, indicating boiling is initiated near the micro-channel outlet. However, Fig. 11a, which corresponds to highly subcooled jets, shows boiling commences at x_{tc3}, not the outlet. Numerical single-phase results show that, while the heat transfer coefficient is lowest near the center of the micro-channel, there is a second local minimum near x_{tc3}. The downstream minimum appears more favorable for nucleation because of both warmer bulk flow and lower pressure near x_{tc3} than at $x = 0$.

The decreasing slope of the boiling curves prior to CHF, albeit small, is indicative of deterioration in heat transfer effectiveness because of local vapor blanket formation. CHF values for the cases in Fig. 11a and b are 276.3 and 213.2 W/cm^2, respectively.

Nucleate boiling inside the hybrid cooling module is fundamentally different from that encountered in conventional micro-channels. In the hybrid module, liquid supplied into the micro-channel from the jet closest to the center undergoes gradual bubble nucleation and growth. However, the micro-channel flow is influenced shortly downstream by the second jet, which can produce rapid condensation and collapse of the bubbles. The micro-channel flow produced by mixing warm upstream fluid with the cooler liquid supplied by the second jet then heats

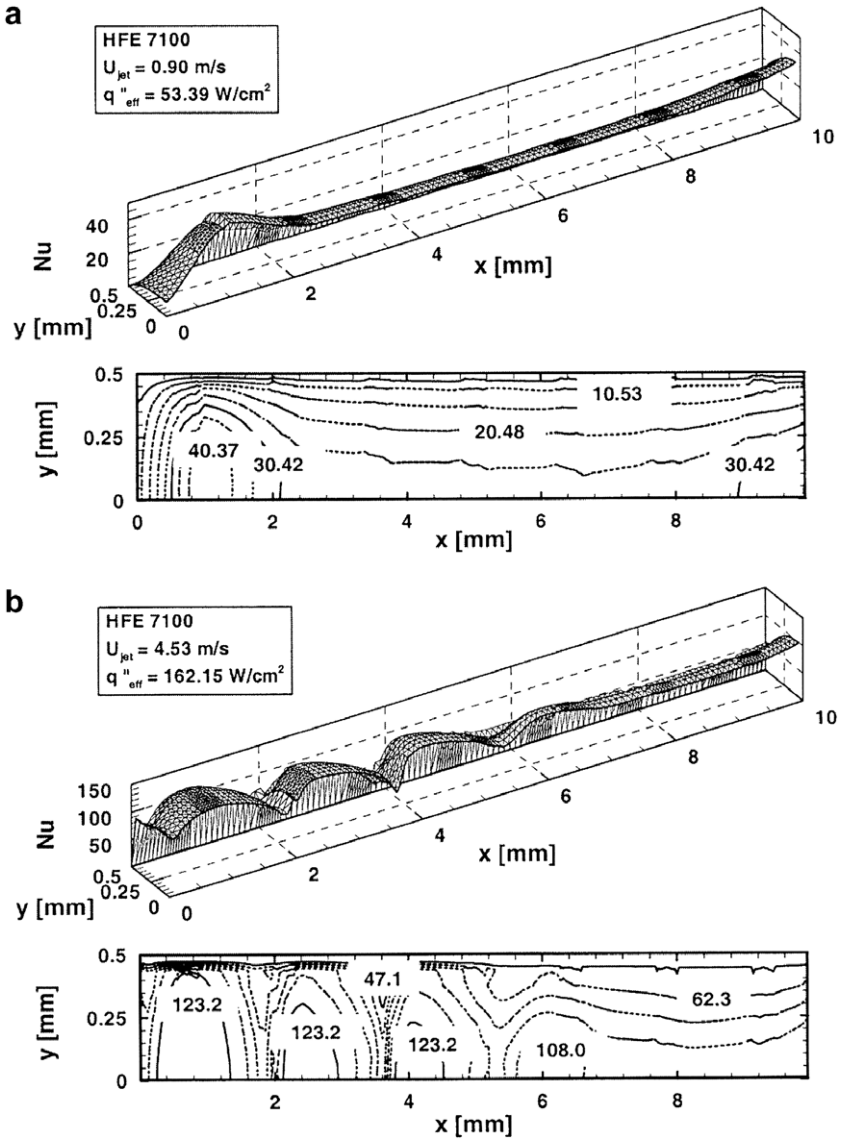

Fig. 10. Numerical predictions of micro-channel bottom wall Nusselt number distribution for (a) $q''_{\text{eff}} = 53.39\ \text{W/cm}^2$ and $U_{\text{jet}} = 0.90\ \text{m/s}$, and (b) $q''_{\text{eff}} = 162.15\ \text{W/cm}^2$ and $U_{\text{jet}} = 4.53\ \text{m/s}$.

up, incurring additional nucleation, until it reaches the third jet. In this manner, the pattern of bubble growth and collapse is repeated along the micro-channel with a relatively mild overall increase in vapor void fraction. This behavior is evidenced in Fig. 11a and b by the relatively small variations in wall temperature along the flow direction.

The effects of jet velocity and subcooling on the boiling characteristics of the hybrid cooling module are shown in Fig. 12a and b, respectively. An area-averaged wall temperature, T_s, is used in these plots. Fig. 12a shows increasing the flow rate delays the onset of boiling and augments single-phase heat transfer considerably. CHF also increases appreciably with increasing flow rate. Fig. 12b shows a relatively weak effect of subcooling on the single-phase region; this effect is the result of relatively mild variations of liquid properties with temperature. However, increasing subcooling delays the onset of boiling to both higher surface temperatures and higher heat fluxes. CHF also increases considerably with increased subcooling because of the subcooled liquid's ability to absorb an appreciable fraction of the supplied heat in the form of sensible energy; subcooled liquid also utilizes condensation to aid in delaying vapor blanket formation.

5.2. Subcooled nucleate boiling region

Several experimental studies have been conducted to investigate the effects of impingement velocity and subcooling on fully developed nucleate boiling. Ma and Bergles [20] showed increasing the subcooling of an R-133 jet caused a slight shift in the boiling data toward lower wall superheat. By varying subcooling of a rectangular FC-72 jet from 10 to 40 °C, Mudawar and Wadsworth [21]

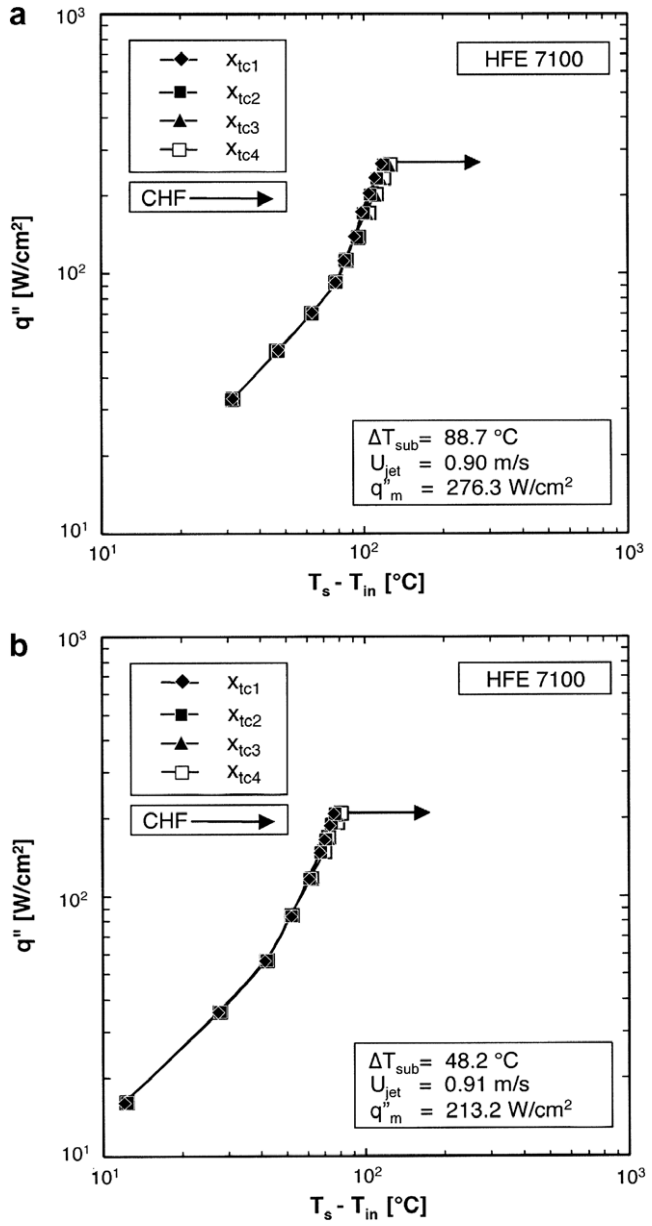

Fig. 11. Boiling curves for four axial wall locations at (a) $\Delta T_{sub} = 88.7$ °C and $U_{jet} = 0.90$ m/s, and (b) $\Delta T_{sub} = 48.2$ °C and $U_{jet} = 0.91$ m/s.

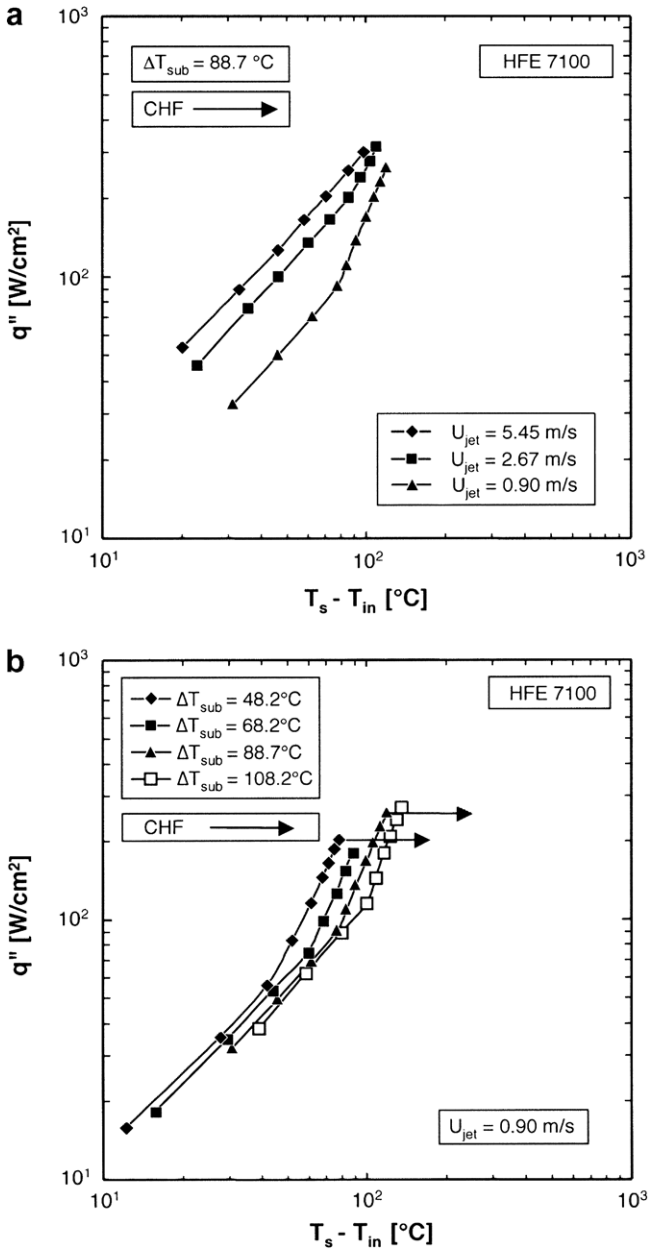

Fig. 12. (a) Flow rate effects on boiling curve at $\Delta T_{sub} = 88.7$ °C. (b) Subcooling effects on boiling curve at $U_{jet} = 0.90$ m/s.

showed a delay in boiling inception, but the nucleate boiling data showed no dependence on subcooling.

Ma and Bergles [20] also showed the nucleate boiling region is independent of jet velocity, an observation shared by Katto and Kunihiro [22] for circular jets. To derive an expression for the nucleate boiling heat transfer coefficient for the present cooling scheme, the following relationship is assumed between heat flux and wall superheat:

$$q''_{eff} = C\Delta T^n_{sat}, \tag{22}$$

where C and n are empirical constants. The subcooling effect is implicit in the above relation since

$$q''_{eff} = h(T_w - T_f) = h(\Delta T_{sat} + \Delta T_{sub}). \tag{23}$$

Combining Eqs. (22) and (23) yields

$$h = \frac{q''_{eff}}{\left(\frac{q''_{eff}}{C}\right)^{1/n} + \Delta T_{sub}}. \tag{24}$$

This expression reveals the two-phase heat transfer coefficient is a function of both q''_{eff} and ΔT_{sub}. The constants C and n are fitted experimentally from the present HFE 7100 data, resulting in the correlation

$$h = \frac{q''}{\left(\frac{q''}{64.81}\right)^{1/3.252} + \Delta T_{sub}}. \tag{25}$$

Fig. 13 compares predictions of this correlation with the present nucleate boiling data. An overall mean absolute

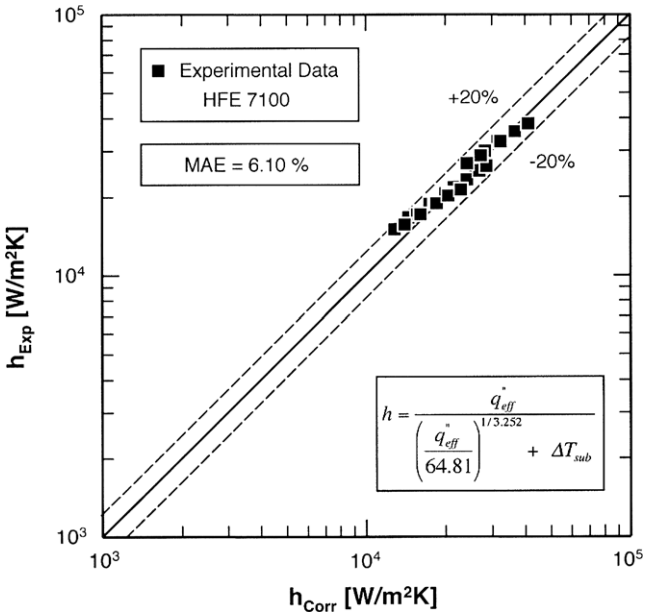

Fig. 13. Comparison of predictions of two-phase heat transfer coefficient correlation with present HFE 7100 data.

error (MEA) of 6.10% demonstrates excellent predictive capability for the present hybrid cooling scheme.

The two-phase heat transfer results of the present study point to many merits of the new hybrid cooling scheme, as well as provide powerful tools for thermal design of a cooling module that utilizes this scheme. However, this study also points to new important phenomena that should be carefully investigated in future work, especially that of a subcooled flow undergoing successive cycles of rapid growth and collapse of bubbles. This behavior is the subject of ongoing efforts by the authors.

6. Conclusions

This study examined the single-phase and two-phase cooling performance of a hybrid micro-channel/micro-jet impingement cooling scheme using HFE 7100 as working fluid. A numerical scheme was developed to explore single-phase flow field and heat transfer characteristics, and predictions were compared to measured temperature distributions. Experiments were also performed to investigate the parametric trends of two-phase cooling performance relative to jet velocity and subcooling, as well as to obtain a correlation for two-phase heat transfer coefficient. Key findings from the study are as follows:

1. Using a systematic technique for defining the extent of the laminar zone in the computational domain, the standard k–ε turbulent model accurately predicts temperature distribution inside the module during single-phase operation.
2. Jet velocity has a profound influence on the single-phase cooling performance of the hybrid cooling module. At high jet velocities, cooling performance is dominated by jet impingement and to a much lesser extent, by micro-channel flow. High jet velocities enable jet liquid to more effectively penetrate the axial micro-channel flow and produce a strong impingement effect at the wall. Peaks in cooling heat flux and heat transfer coefficient are encountered below the jet centerlines. Low velocity jets, on the other hand, are too weak to penetrate the micro-channel flow and the influence of the jets is greatly compromised compared to micro-channel flow.
3. Bubble nucleation, growth, departure, and coalescence along the micro-channel in the hybrid scheme are fundamentally different from those encountered in conventional micro-channels. In the hybrid scheme, subcooled jet fluid can cause rapid condensation and collapse of bubbles formed upstream. Therefore, this scheme involves repeated regions of bubble growth followed by collapse, rather than the continuous bubble growth common to conventional micro-channel flow. By reducing void fraction along the micro-channel, the hybrid scheme contributes greater wall temperature uniformity.
4. Increasing subcooling and/or flow rate delay the onset of boiling to higher heat fluxes and higher wall temperatures. CHF also increases considerably with increased subcooling as liquid is able to absorb a large fraction of the supplied heat in the form of sensible heat, and better condensation resists vapor blanket formation.
5. A new correlation for the nucleate boiling region, which accounts for subcooling, fits the present HFE 7100 data with a mean absolute error of 6.10%.

Acknowledgement

The authors are grateful for the support of the Office of Naval Research (ONR) for this study.

References

[1] I. Mudawar, Assessment of high-heat-flux thermal management schemes, IEEE Trans. – Compon. Pack. Technol. 24 (2001) 122–141.
[2] M.K. Sung, I. Mudawar, Single-phase hybrid micro-channel/micro-jet impingement cooling, Int. J. Heat Mass Transfer, in press.
[3] A.G. Fedorov, R. Viskanta, Three-dimensional conjugate heat transfer in the microchannel heat sink for electronic packaging, Int. J. Heat Mass Transfer 43 (2000) 399–415.
[4] W. Qu, I. Mudawar, Experimental and numerical study of pressure drop and heat transfer in a single-phase micro-channel heat sink, Int. J. Heat Mass Transfer 45 (2002) 2549–2565.
[5] E. Baydar, Y. Ozmen, An experimental and numerical investigation on a confined impinging air jet at high Reynolds numbers, Appl. Therm. Eng. 25 (2005).
[6] J.M.M. Barata, D.F.G. Durao, M.V. Heitor, J.J. McGuirk, On the analysis of an impinging jet on ground effects, Exp. Fluids 15 (1973) 117–129.
[7] T.J. Craft, L.J.W. Graham, B.E. Launder, Impinging jet studies for turbulence model assessment – II. An examination of the performance of four turbulence models, Int. J. Heat Mass Transfer 36 (1993) 2685–2697.
[8] M.B. Bowers, I. Mudawar, High flux boiling in low flow rate, low pressure drop mini-channel and micro-channel heat sinks, Int. J. Heat Mass Transfer 37 (1994) 321–332.

[9] W. Qu, I. Mudawar, Measurement and prediction of pressure drop in two-phase micro-channel heat sinks, Int. J. Heat Mass Transfer 46 (2003) 2737–2753.
[10] J. Lee, I. Mudawar, Two-phase flow in high-heat-flux micro-channel heat sink for refrigeration cooling applications: Part I – pressure drop characteristics, Int. J. Heat Mass Transfer 48 (2005) 928–940.
[11] C. Yang, A.A.O. Tay, H. Xue, An experimental study of liquid jet impingement cooling of electronic components with and without boiling, in: Proceedings of the Advances in Electronics Material and Packaging, IEEE, November 19–22, Jeju Island, Korea, 2001, pp. 369–375.
[12] D.H. Wolf, F.P. Incropera, R. Viskanta, Local jet impingement boiling heat transfer, Int. J. Heat Mass Transfer 39 (1996) 1395–1406.
[13] D.C. Wadsworth, I. Mudawar, Cooling of a multichip electronic module by means of confined two-dimensional jets of dielectric liquid, ASME J. Heat Transfer 112 (1990) 891–898.
[14] Fluent 6.2.16, User's Guide, Fluent Inc., Lebanon, NH, 2005.
[15] Gambit 2.2.30, User's Guide, Fluent Inc., Lebanon, NH, 2006.
[16] B.E. Launder, D.B. Spalding, The numerical computation of turbulent flows, Comput. Meth. Appl. Mech. Eng. 3 (1974) 269–289.
[17] S.V. Patankar, Numerical Heat Transfer and Fluid Flow, Hemisphere, Washington, DC, 1980.
[18] F.P. Incropera, Liquid Cooling of Electronic Devices by Single-phase Convection, Wiley, New York, 1999.
[19] E.J. Watson, The radial spread of a liquid over a horizontal plane, J. Fluid Mech. 20 (1964) 481–499.
[20] C.F. Ma, A.E. Bergles, Jet impingement nucleate boiling, Int. J. Heat Mass Transfer 29 (1986) 1095–1101.
[21] I. Mudawar, D.C. Wadsworth, Critical heat flux from a simulated chip to a confined rectangular impinging jet of dielectric liquid, Int. J. Heat Mass Transfer 34 (1991) 1465–1479.
[22] Y. Katto, M. Kunihiro, Study of the mechanism of burn-out in boiling system of high burn-out heat flux, Bull. JSME 16 (1973) 1357–1366.